

## QuickPALM: 3D real-time photoactivation nanoscopy image processing in ImageJ

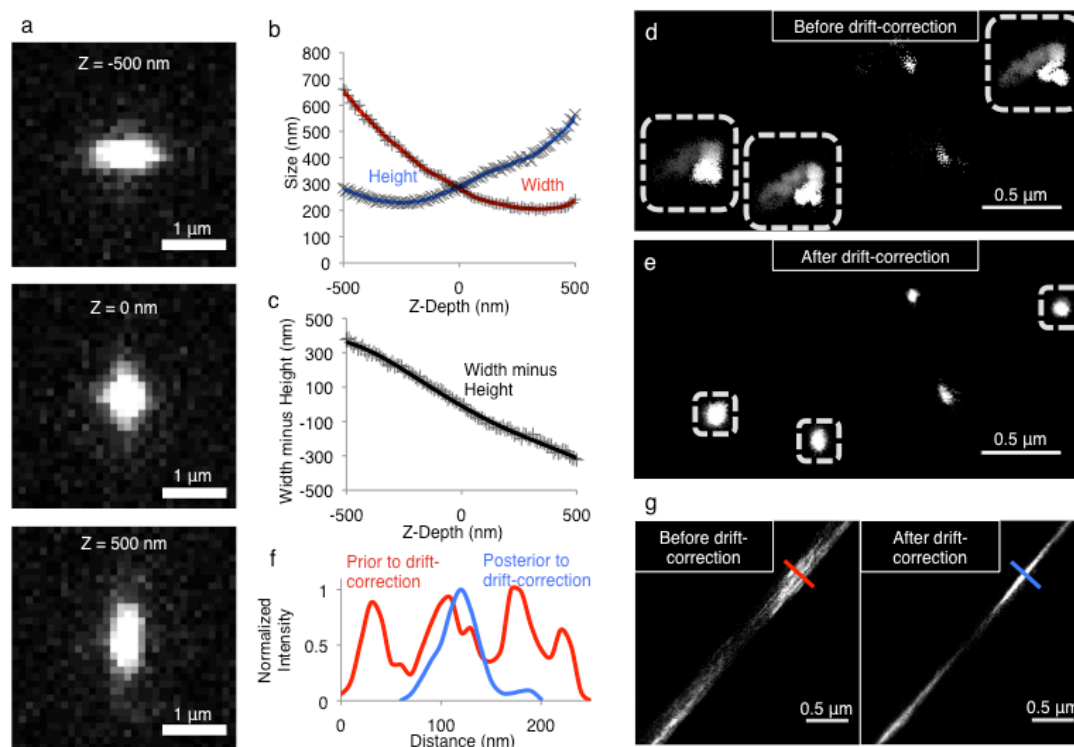
Ricardo Henriques, Mickael Lelek, Eugenio F Fornasiero, Flavia Valtorta, Christophe Zimmer & Musa M Mhlanga

Supplementary figures and text:

<b>Supplementary Figure 1</b>	3D localization and drift correction using QuickPALM.
<b>Supplementary Figure 2</b>	Microscope setup for 3D imaging.
<b>Supplementary Methods</b>	
<b>Supplementary Note 1</b>	Design and operation of QuickPALM
<b>Supplementary Discussion</b>	Overview of QuickPALM performance

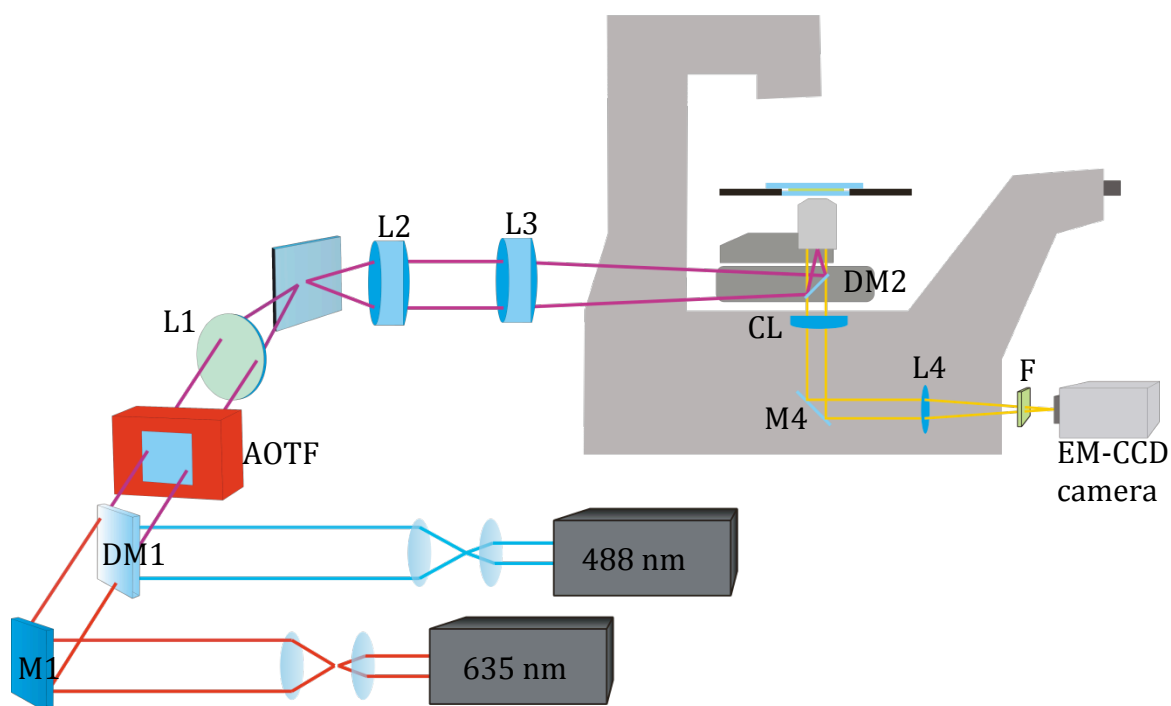
*Note: Supplementary Software 1–2 and Supplementary Video 1 are available on the Nature Methods website.*

## Supplementary Figure 1: 3D localization and drift correction using QuickPALM



**(a)** Image sequence showing a single fiduciary sub-diffraction bead observed at different depths with an astigmatic configuration. Note the changes in the width to height ratio. **(b)** Measured width and height as a function of  $Z$ . Each data point represents the nine-point moving average from three beads. **(c)** Width minus height as a function of  $Z$  based on the values of **(b)**; the black line shows a 4<sup>th</sup> order polynomial fit, which is used to extract the  $Z$  position of newly detected sub-diffraction spots. **(d)** Overlay of computed bead positions acquired during the image sequence showing lateral drift (dot brightness is proportional to the bead intensity, and decays over time due to photobleaching). **(e)** Same as **(d)** after drift-correction. **(f,g)** Drift effect on an image of microtubules creating the misleading appearance of multiple-filaments. **(f)** A line profile of the red and green cross-sections in **(g)** before (green) and after (red) drift-correction.

## Supplementary Figure 2: Microscope setup for 3D imaging



Schematic of the microscope used in this work. Laser light from two lasers is combined using the mirror (M1) and the dichroic beamsplitter (DM1). The two beams are switched using an acousto-optic tunable filter (AOTF) and a series of lenses (L1-L3) directs the beams into the objective. Fluorescent light from the sample crosses the dichroic beamsplitter (DM2) and transverses a cylindrical lens (CL) that introduces an astigmatic aberration into the image allowing us to perform the 3D localization of sub-diffraction particles, the correspondent light is then redirected by a mirror (M4), magnified by a tube-lens (L4) and filtered by an emission filter (F) before reaching the camera.

## Supplementary Methods

### *Slide treatment*

Coverslips were prepared as previously described<sup>1</sup>. Briefly, round 25x0.17-mm coverslips (Fisher Scientific, Pittsburgh, PA) were cleaned in porcelain racks for 18h in concentrated nitric acid, washed several times in tissue-culture-grade water and sterilized with dry heat (225° C for 8h) in a clean oven.

### *Hippocampal neuron cell culturing*

Primary neuronal cultures were prepared from the hippocampi of Sprague-Dawley E18 rat embryos (Charles River Italica, Calco, Italy) as previously described<sup>2</sup>. Briefly, after euthanization of the pregnant mother, E18 rat embryos were isolated, and hippocampi were dissected in cold calcium- and magnesium-free Hank's balanced salt solution (HBSS; Gibco, United Kingdom) supplemented with 5 mM HEPES pH 7.4. Hippocampi were washed several times in HBSS and dissociated in 0.25 % trypsin (Gibco, United Kingdom) for 15 minutes at 37°C. After trypsin removal, neurons were plated in minimum essential medium with Earle's salts (MEM; Gibco, United Kingdom) containing 10% Horse serum during the time necessary for adhesion, and subsequently co-cultured for 3 days with primary astrocytes in N2 supplemented MEM.

### *Cell labeling*

Neurons were fixed for 15 minutes at RT with 4% paraformaldehyde, 4% sucrose in 120 mM sodium phosphate buffer (pH 7.4) supplemented with 2 mM EGTA. After fixation, cells were washed in phosphate buffered saline (PBS) for 0.5h and incubated with anti neuronal tubulin beta-III antibody (Covance, United Kingdom) diluted 1:100 in goat serum buffer (450 mM NaCl, 20 mM phosphate buffer, 15% goat serum, and 0.3% Triton X-100) for 2h at RT. Upon primary antibody incubation cells were washed in PBS for 0.5h and incubated with Cy5 conjugated donkey anti rabbit antibody (Jackson ImmunoResearch, West Grove PA) for 1h at RT. Fluorescent beads (100nm diameter) of a similar emission wavelength, were mounted with the sample as fiduciary landmarks.

### *Slide preparation for imaging and acquisition.*

Slides were sealed in a Parafilm® M gasket. Imaging was performed in a "reactive oxygen scavenger photo-switching buffer" as previously described<sup>3</sup>. The buffer contains 0.5 mg/mL glucose oxidase (Sigma), 40 µg/ml catalase (Roche Applied Science), 10% w/v glucose and 50 mM of β-mercaptoethylamine in PBS (pH 7.4). 150,000 fluorescence images were acquired with a 50 ms exposure time in laser-excitation widefield. The sample was excited with a 635 nm laser with the power adjusted for optimal and fast bleaching of activated Cy5 molecules while a 488 nm laser was pulsed at decreasing intervals to stochastically reactivate bleached Cy5 molecules and maintain an optimal visible number of emitting molecules in the field of view.

## Microscope components and setup

Laser light from the two lasers (EXLSR-635C-60mW and CYAN- 488-100mW, Spectra-Physics, Japan) is combined using the mirror M1 and the dichroic beamsplitter DM1 (LM01-503-25, Semrock, Rochester, NY, USA). The switching between the activation wavelength and the excitation wavelength and intensity control of each laser are performed via an acousto-optic tunable filter (AOTFnC-400.650, A-A Opto-Electronic, Orsay Cedex, France). Before the injection of the laser beams inside the microscope, they are widened by a telescope consisting of the achromatic doublet lenses L1 and L2 and focused into the back focal plane of the objective (CFI Apochromat, 100x, NA 1.49, Nikon, Japan) by the achromatic doublet lens L3. The far red fluorescence emission is collected by the same objective, separated from the illumination light by a quad-band line dichroic mirror DM2 (FF416/500/582/657-DiO1, Lot # 709240-709242 Semrock, Rochester, NY, USA and latter filtered with a dual band pass Filter F (FF01-577/690-25, Lot # 307339-207360 Semrock, Rochester, NY, USA) being finally detected by an EM-CCD camera (Ixon DV887ECS-BV, Andor, Belfast, Northern Ireland) via the mirror M4. An additional lens L4 is used to achieve a final imaging magnification of 100 to 150 times yielding a pixel size from 160 to 106 nm. 3D imaging is performed by adding a cylindrical lens CL (RCX cylindrical lens 10m focal length, CVI Melles Griot) before L4 in order to create an astigmatism, whereby the detected spot shape depends on the fluorophore depth<sup>4</sup> – most microscope bodies have a polarizer insertion slider immediately below the filter cube wheel that can be cleverly adapted as a cavity to insert the cylindrical lens (see **Sup. Fig. 2**).

## Supplementary Note: Design and operation of QuickPALM

### *Particle detection, localization and visualization*

Particle detection and localization takes advantage of all available CPUs on the processing computer through the use of a thread manager (see “Thread Manager” in **Sup. Note Fig. 1**) that distributes the processing jobs between available free CPUs or buffers the acquisition while waiting for these to become free.

Within each thread a new unprocessed image is collected (see “Open next image” in **Sup. Note Fig. 1**) and the noise is characterized by calculating the standard deviation on a small area of 13x13 pixels centered on the minimum intensity pixel of the image. It is assumed that due to the stochastic nature of a PALM or STORM image there is a low probability of having a blinking molecule in the immediate neighborhood of this point. A band-pass filter is then applied to provide noise reduction and background correction on the overall image (see “Filtering” in **Sup. Note Fig. 1**). Initially the image is convolved with a Gaussian kernel of sigma equal to 0.5 pixels and subtracted to a convolution of the original image with a Gaussian kernel of sigma with twice the maximum FWHM given by the user, thus both reducing the noise frequencies and background of the overall image without any visible decrease of the localization accuracy.

The image is then searched for the maximum intensity pixel, the surrounding pixels to this point are selected if within a square window of size twice the maximum *FWHM* whose values are above a relative threshold to the local peak intensity (see “Get brightest spot” in **Sup. Note Fig. 1**). The local SNR is calculated as the division between the mean intensity of the selected pixels and the noise standard deviation. If this value is below the minimum SNR given by the user then the process for this image is halted (see “Compare against SNR” in **Sup. Note Fig. 1**).

Before the spot is registered as a potentially valid particle it needs to pass the following tests: image edge – if a part of the intensity profile of the spot is obscured by the image edge; saturation/clamping – if the intensity of the local spot is not saturated; already analyzed region overlapping – if any of the pixels of the spot overlap with the region of an already previously analyzed spot on the same image. If these tests are correctly passed the algorithm proceeds to calculate the center of the spot coordinates ( $c_x$ ,  $c_y$ ) as given by the center of mass formulas:

$$c_x = \frac{\sum_{i,j} s_{i,j} x_{i,j}}{\sum_{i,j} s_{i,j}}$$
$$c_y = \frac{\sum_{i,j} s_{i,j} y_{i,j}}{\sum_{i,j} s_{i,j}}$$

where  $i$ ,  $j$  are the  $x$ -axis and  $y$ -axis indices for each pixel within the spot,  $x_{i,j}$  and  $y_{i,j}$  are the coordinates of the pixel in nanometers and  $s_{i,j}$  the intensity of the pixel (see “Get center of mass” in **Sup. Note Fig. 1**). The spot shape is then characterized by calculating the parameters:

$$\begin{aligned}\sigma_l &= \sum_{i,j} s_{i,j} (c_x - x_{i,j}) / \sum_{i,j} s_{i,j}, \text{ where } (i,j) \in \{(i,j) \mid x_{i,j} < c_x\} \\ \sigma_r &= \sum_{i,j} s_{i,j} (x_{i,j} - c_x) / \sum_{i,j} s_{i,j}, \text{ where } (i,j) \in \{(i,j) \mid x_{i,j} \geq c_x\} \\ \sigma_a &= \sum_{i,j} s_{i,j} (c_y - y_{i,j}) / \sum_{i,j} s_{i,j}, \text{ where } (i,j) \in \{(i,j) \mid y_{i,j} < c_y\} \\ \sigma_b &= \sum_{i,j} s_{i,j} (y_{i,j} - c_y) / \sum_{i,j} s_{i,j}, \text{ where } (i,j) \in \{(i,j) \mid y_{i,j} \geq c_y\}\end{aligned}$$

if the spot arises from a single diffraction limited particle and if the PSF is symmetric then the particles can approximate to a Gaussian PSF model where in the absence of astigmatism  $\sigma_l \approx \sigma_r \approx \sigma_a \approx \sigma_b$  or otherwise in its presence  $\sigma_l \approx \sigma_r$  and  $\sigma_a \approx \sigma_b$ . We can calculate the particle x-, y-axis symmetry as

$$S_x = 1 - \frac{|\sigma_l - \sigma_r|}{\sigma_l + \sigma_r}; \quad S_y = 1 - \frac{|\sigma_a - \sigma_b|}{\sigma_a + \sigma_b}$$

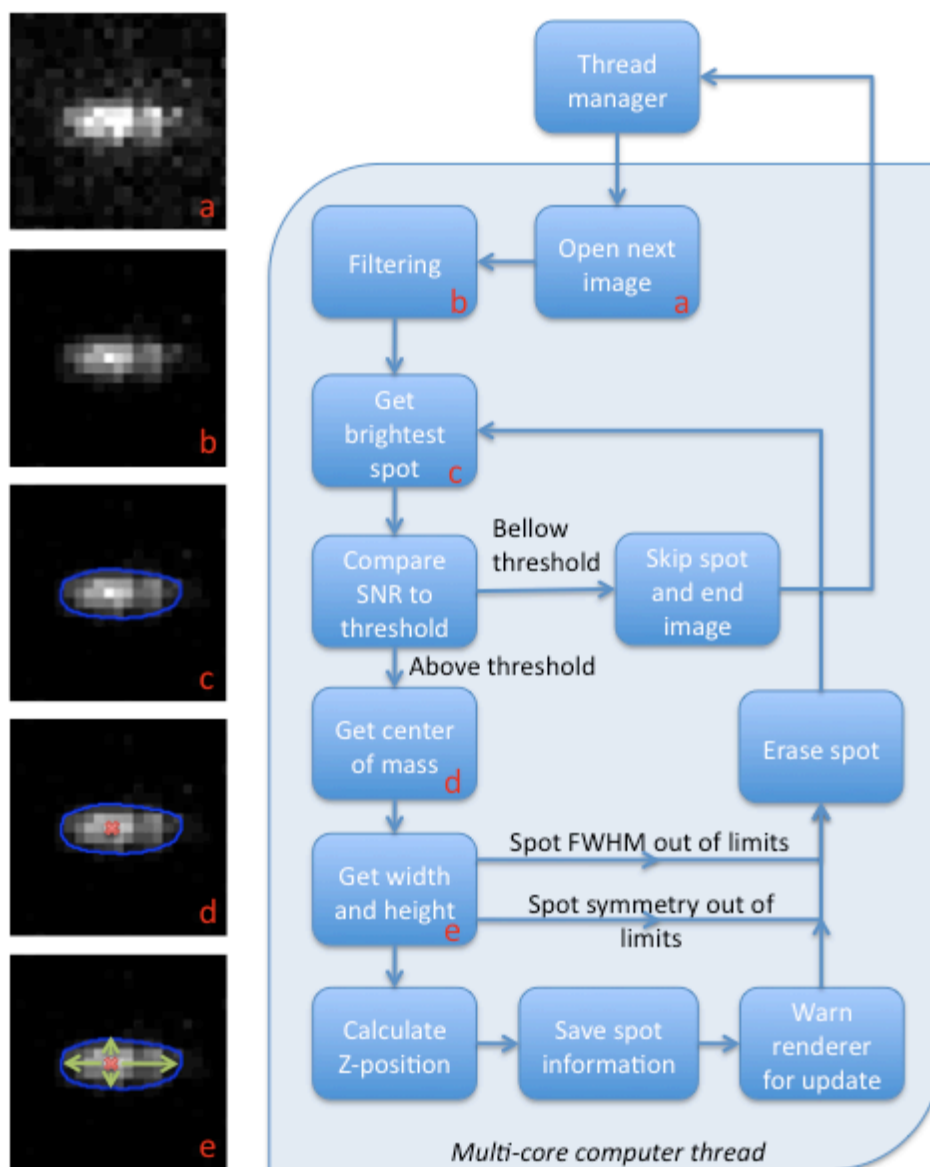
for a single diffraction limited particle, one expects  $S_x \approx 1$  and  $S_y \approx 1$  with or without astigmatism. The lateral *FWHM* along each axis (see “Get width and height” in **Sup. Note Fig. 1**) can be defined as

$$\begin{aligned}FWHM_x &= 2.354(\sigma_l + \sigma_r)/2 \\ FWHM_y &= 2.354(\sigma_a + \sigma_b)/2\end{aligned}$$

in the absence of astigmatism one expects

$$FWHM_x \approx FWHM_y \approx 2.354(\sigma_0/2) \text{ with } \sigma_0 = 0.225(\lambda/NA);^5$$

it then becomes possible to test if the particle obeys a symmetry limit or if the *FWHM* values are within assigned margins given by the user in the graphical interface. The z-position of the particle is extracted by comparing the width minus height (*WmH*) of the particle calculated as  $WmH = FWHM_x - FWHM_y$  against the values on a z-calibration table (**Sup. Note Fig. 2**) through linear interpolation of the closest *WmH* values on the table and associated *Z*-coordinates (see “Calculate Z-position” in **Sup. Note Fig. 1**). Finally if all tests are passed, the information for the spot is saved (“Save spot information” in **Sup. Fig. S1**).



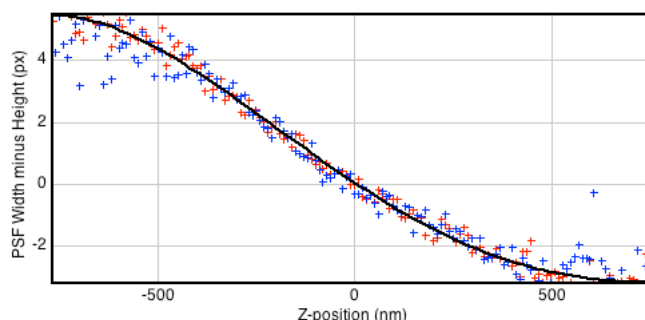
**Supplementary Note Figure 1.** Flow-chart of particles detection, localization and visualization within QuickPALM. Images in left column schematically represent the corresponding steps on the flow-chart labeled with the same inset letter.

### *3D particle localization by comparison with an experimental calibration table*

In order for QuickPALM to localize particles in the z-axis it needs to have prior-information on the astigmatic distortion, this is done by first acquiring a sequence of calibration images with the astigmatic lens<sup>4</sup> featuring sub-diffraction beads. Ideally these images are acquired at regular 10 nm *Z* intervals with the help of a piezo *Z*-motor. It should be possible to observe the width and height change of the *PSF* as a function of *Z*. QuickPALM is able to generate this calibration table, however, the user needs to first manually select which beads to use for calibration with the help of the “ROI Manager”. After this selection QuickPALM calculates the position, width and height of each selected bead through the “Get center of mass” and “Get width and



height” methods discussed before and generates a plot of *Width-Height* vs. *Z* (**Sup. Note Fig. 2**).



**Supplementary Note Figure 2.** Example plot of the width minus height change for bead particles corrupted by astigmatism as a function of the z-position as calculated by QuickPALM. Crosses are measured values for each selected bead, the curve represents a 4<sup>th</sup> order polynomial fit to the data. The fitted values are saved as a calibration table and later used by the “Get Z-position” method previously described to estimate the z-position for each detected particle.

#### *Drift calculation and correction*

Drift correction is accomplished after the user has pre-defined one or more regions of interest around isolated spot clusters corresponding to either landmark beads added to the sample or individual molecules (**Sup. Note Fig. 3a**). The algorithm then calculates the distribution center  $c_{r,w}$  in each axis (**Sup. Note Fig. 3b**) for the selected clusters indexed by  $r$  ( $w$  represents either the x-, y- or z-axis):

$$c_{r,w} = \sum_t s_{r,t} w_{r,t} / \sum_t s_{r,t}$$

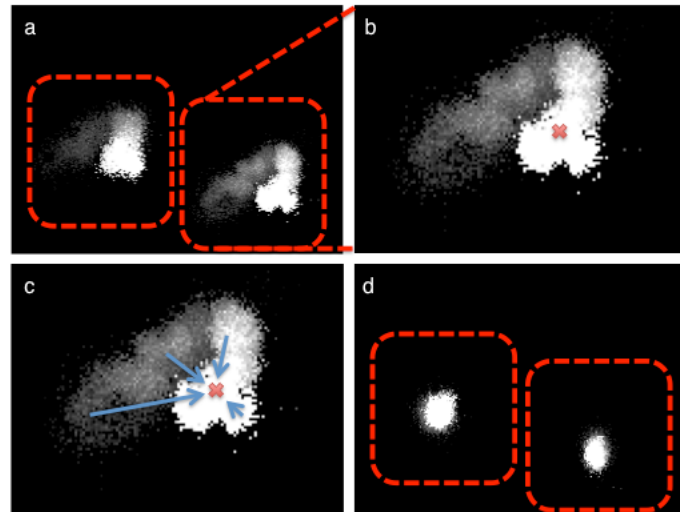
$$d_{w,t} = \sum_r s_{r,t} (c_{r,w} - w_{r,t}) / \sum_t s_{r,t}$$

where  $t$  is the time-point index for each detected spot within the cluster,  $s_{r,t}$  the intensity for that spot and  $w_{r,t}$  the localization of spot center. The joint displacement between each element of the cluster and its center is also calculated (**Sup. Note Fig. 3c**) as  $d_{w,t}$ . Due to the possibility of missing detections, the displacement track  $d_{w,t}$  might not contain the displacement information for all time-points. In order to correct this, we linearly interpolate the missing values and iteratively update both the cluster centers and displacements as follows:

$$\hat{c}_{r,w}^{i+1} = \sum_t s_{r,t} (w_{r,t} + \hat{d}_{w,t}^i) / \sum_t s_{r,t}$$

$$\hat{d}_{w,t}^{i+1} = \sum_r s_{r,t} (\hat{c}_{r,w}^{i+1} - w_{r,t} - \hat{d}_{w,t}^i) / \sum_r s_{r,t}$$

where  $\hat{c}_{r,w}^{i+1}$  and  $\hat{d}_{w,t}^{i+1}$  are the corresponding cluster center and joint displacement estimations for the  $i$ -th iteration. The updates are performed until convergence is achieved. The particle position data is then corrected by subtracting the corresponding displacement value to each particle position (**Sup. Note Fig. 3d**).



**Supplementary Note Figure 3.** Drift correction with QuickPALM through the selection of individual spot clusters. **(a)** Identification and selection of individual spot clusters caused by the repetitive detection of beads or fluorophore clusters over time. **(b)** Calculation of the center of mass of the spot cluster. **(c)** Estimation of the displacement of each spot in regards to the cluster center. **(d)** Plot of the spot clusters after drift correction.

## Supplementary Discussion: Overview of the QuickPALM performance

During a typical image acquisition of 512x512 frames in a PALM/STORM experiment, the frame-rate hard-limit imposed by the readout speed of the camera, such as in the case of the EM-CCD technology, is on the order of 32ms. QuickPALM has a typical processing time of 30-50ms that may vary depending on the sample complexity and processing computer characteristics (**Fig. 1a**). Notwithstanding, this standard processing speed allows real-time super-resolution image reconstruction, albeit at a minor loss in localization accuracy compared to Gaussian fitting methods<sup>4</sup>. In practice, our software automatically processes incoming low-resolution images streamed on the hard drive during image acquisition and accumulates the computed positions into a real-time super-resolution reconstruction. Without real-time reconstruction, imaging parameters such as activation/excitation intensities often need to be optimized by trial and error after multiple suboptimal experiments. Our method allows the dynamic inspection of sample behavior and the adjustment of acquisition parameters “on the fly” for optimal imaging.

Real-time reconstruction and the integration of software for parallel processing and acquisition, in conjunction with an open source platform, allows super-resolution imaging modalities to be broadly adopted and extended. Since processing and reconstruction can occur in real-time and on a separate machines, data-driven decisions can be used in real-time to control actuators. For example, spatial light modulators could be used to locally optimize the activation laser power and ensure uniform blinking probabilities, thus minimizing acquisition time, as required for live super-resolution imaging<sup>6,7</sup>. In a further example, initial super-resolution images reconstructed from a limited number of frames may identify the presence of an event of interest and inform the decision to continue PALM/STORM imaging at this location with real-time visualization - or search for another region-of-interest. This would be an important feature to study events such as host-pathogen interactions in high-throughput screening approaches<sup>8</sup>.

## References

1. S. Kaech and G. Banker, *Nat Protoc* **1** (5), 2406 (2006).
2. G. A. Banker and W. M. Cowan, *Brain Res* **126** (3), 397 (1977).
3. M. Heilemann, S. van de Linde, M. Schuttpelz et al., *Angew Chem Int Ed Engl* **47** (33), 6172 (2008).
4. B. Huang, W. Wang, M. Bates et al., *Science* **319** (5864), 810 (2008).
5. B Zhang, J Zerubia, and JC Olivo-Marin, *Applied Optics* **46** (10), 1819 (2007).
6. H. Shroff, C. G. Galbraith, J. A. Galbraith et al., *Nat Methods* **5** (5), 417 (2008).
7. S. Manley, J. M. Gillette, G. H. Patterson et al., *Nat Methods* **5** (2), 155 (2008).
8. R. Henriques and M. M. Mhlanga, *Biotechnol J* **4** (6), 846 (2009).